PMSG-Based Wind Energy Conversion Systems Integration Into DC Microgrids With a Novel Compact Converter

JAVAD KHODABAKHSH[iD]**, (Student Member, IEEE),**
EBRAHIM MOHAMMADI[iD]**, (Member, IEEE),**
AND GERRY MOSCHOPOULOS[iD]**, (Senior Member, IEEE)**
Electrical and Computer Engineering Department, Western University, London, ON N6A 3K7, Canada

Corresponding author: Javad Khodabakhsh (jkhodaba@uwo.ca)

ABSTRACT DC microgrids (DC-MGs) are recognized as an efficient alternative for common AC-MGs. DC-MGs need fewer power electronic converters since most of distributed generation (DG) units and electronic loads operate with DC voltage. The integration of DGs that generate AC voltage, such as wind energy conversion systems (WECSs) into DC-MGs, however, requires an AC-DC conversion unit to perform AC-DC conversion and galvanic isolation and to control the WECS. Typically, two separate cascaded converters are used to perform such functions, which increases the cost and size of DC-MGs. In this paper, an isolated single-stage AC-DC converter is proposed that is able to perform all the required function of a WECS AC-DC conversion unit, to overcome the drawbacks of the two-converter structure. First, the operation of the proposed converter and its features as a single unit are described. The operation of the WECS with the proposed converter is then studied. A design procedure for both the steady-state and dynamic operation of the converter is developed based on a mathematical model. Experimental results obtained from a scaled-down prototype converter are also presented to confirm the feasibility of the proposed converter as a single unit. The complete WECS operation is verified by the simulation results of the aerodynamic, mechanical, and electrical system models, using MATLAB/SIMULINK.

INDEX TERMS PMSG, wind energy conversion system, galvanic isolation, ac-dc conversion, dc microgrids.

I. INTRODUCTION

Microgrids (MGs) are promising solutions for reducing power transmission costs, power losses [1], and for increasing power system resiliency [2]. MGs are a cluster of loads and generation units that are located in a small geographical area. AC-MGs are the dominant type of MGs because they can easily interface to a bulk AC power system as a reliable energy source. DC-MGs, however, came into prominence, especially in islanded microgrids, because they are more efficient in interfacing with most renewable energy distributed generators (DGs), energy storage systems (ESSs), and electronic loads [3]–[5]. Moreover, DC-MGs do not have problems related to reactive power and power quality [6]–[8].

Small-scale wind energy conversion systems (WECSs) with a permanent magnet synchronous AC generator (PMSG)

The associate editor coordinating the review of this manuscript and approving it for publication was Dongbo Zhao.

and fixed pitch (e.g., Bergey Excel-S 10 kW [9]) are widely used as renewable energy resources in DC-MGs [10]–[13]. An AC-DC conversion unit is thus required to connect an AC-PMSG to a DC microgrid. Unlike simple AC-DC converters, AC-DC conversion units in WECSs are essentially PMSG drive systems that must perform functions such as AC-DC power conversion, power factor correction (PFC) to reduce the ohmic power losses in the generator [14], maximum power point tracking (MPPT), and galvanic isolation between the AC part of the WECS and the DC-MG for safety reasons [15], [16].

Typically, two separate cascaded converters are used to perform the stated functions. A front-end AC-DC converter that performs AC-DC conversion, PFC, and MPPT, and a back-end DC-DC converter that is used to galvanically isolate the AC and the DC part of the systems. This structure is called a two-stage AC-DC converter. The block diagram of a typical WECS with a two-stage converter alongside its
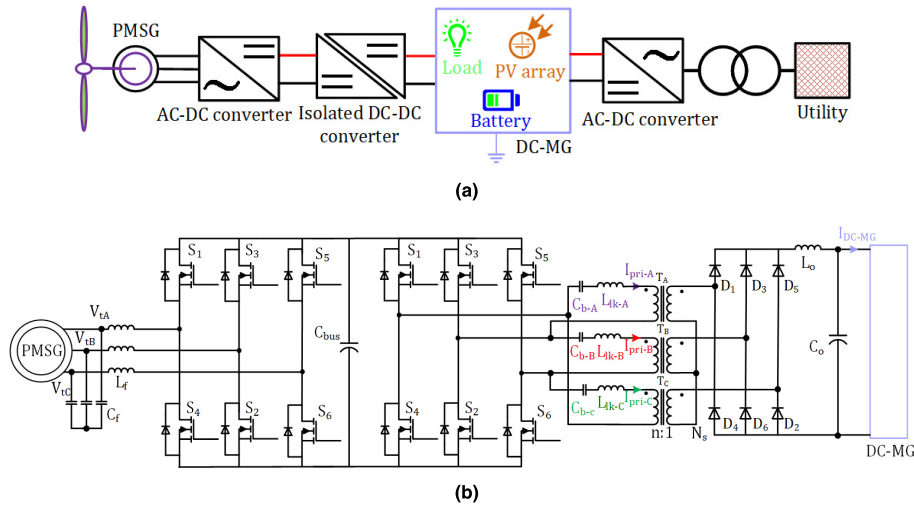
FIGURE 1. WECS unit integration in a DC-MG (a) proposed configuration in [15], [16], (b) circuit diagram of a typical two-stage AC-DC converter.

circuit diagram is shown in Fig. 1. This two-stage converter is an expensive solution because it has two power stages with 12 switches and two controllers.

The cost of the power electronic converter is a considerable portion of the overall cost of small-scale WECSs in comparison with large-scale wind farms [17]. Any cost reduction in the power electronic converters will thus significantly reduce the overall cost of WECSs.

Isolated single-stage AC-DC converters that are introduced for power supply applications as simpler, lighter, and less expensive converters also can be used in AC-DC conversion units of WECSs. These converters share the active switches between the front-end AC-DC converter and the back-end DC-DC converter stages and a single controller is used to control the converter. Some modifications, however, are required to use a single-stage AC-DC converter for WECS application because the AC-DC converter functionalities in a WECS are more complex than those in a power supply application.

An isolated single-stage AC-DC converter for WECS should perform the required control for the WECS on top of AC-DC conversion, PFC correction, and galvanic isolation. In order to investigate the possibility of using isolated AC-DC converters for a WECS, a brief review of such converters is presented as follows:

- Single-stage AC-DC converters with a fixed duty cycle operation [18], [19]: In these types of converters, the input power is controlled by operating converter switches with a fixed duty cycle over the full input voltage cycle and PFC is naturally performed with the sinusoidal envelope of a train of triangle current waveform. This method is simple to implement, but the input current has high peak components that increase the peak current stress on the components and cause EMI noise, and thus can be used only for low power applications < 2kW. Moreover, it is very difficult to control the input power for MPPT and power regulation applications

since a high bandwidth current sensor and voltage sensor are needed to calculate the real-time power.
- Single-stage AC-DC converters with a matrix converter topology[20]–[22]: In these types of converters, the input current is smoother than converters with a fixed duty cycle. These converters, however, require a significant number of switches and their control strategy is too complicated.
- Single-stage AC-DC converters with a diode bridge at the input stage [23], [24]: In these types of converters, the diode bridge has high conduction losses; thus, their application is limited to low power applications.
- Single-stage AC-DC converters with non-standard control methods [25]: In these types of converters, complicated control methods (i.e., variable duty cycle and frequency) are used, thus real-time power calculation and the implementation of MPPT is difficult.
- Single-stage AC-DC converters based on the standard voltage source converter (VSC) structure [26]: In these types of converters, the input current is continuous and the control system is operation is well-known for both the scholars and engineers; this converters are thus promising for use in WECS applications.

It should be noted that the proposed converter in [26] was originally proposed for power supply applications. The main contributions of this paper are as follows:

- Three isolation transformers are used to extend the operating power range of the converter proposed in [26].
- A new control system is proposed that enables the isolated the single-stage AC-DC converter in [26] to perform MPPT and power regulation in addition to all the control objectives in [26].
- A design procedure for the components and control system is developed by using a mathematical model of the proposed converter.
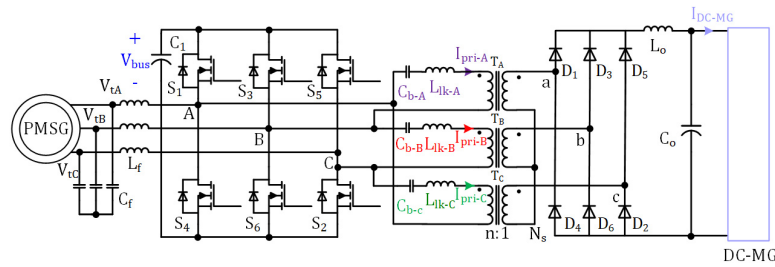
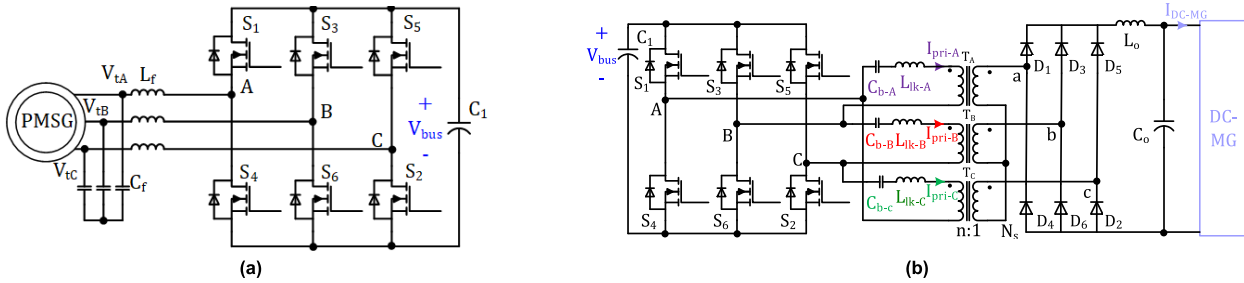**FIGURE 2.** Circuit diagram of proposed single-stage AC-DC converter.

FIGURE 3. Proposed WECS unit converter stages. (a) AC-DC sub-converter, (b) DC- DC sub-converter.

- A scaled-down prototype of the proposed converter was built to confirm the feasibility of the converter as a single unit.
- A comprehensive aerodynamic, mechanical, and electrical simulation was performed in MATLAB/SIMULINK to demonstrate the converter effectiveness in a WECS.

The following parts of this paper are organized as follows. In Section II, the proposed converter topology and operation basics are explained. In Section III, the proposed control system for the converter is explained. In Section IV, experimental results from a scaled-down converter are presented to verify converter feasibility as a single unit, and simulation results of the aerodynamic, mechanical, and electrical systems are shown to verify the effectiveness of the proposed converter in a complete WECS. Conclusions presented in Section V.

II. THE PROPOSED CONVERTER
The proposed isolated single-stage AC-DC converter is shown in Fig. 2. The converter consists of an input filter L_f and C_f, a six-switch three-phase inverter ($S_1 - S_6$), a capacitor in the intermediate bus (C_1), three dc blocking capacitors ($C_{b-A}, C_{b-B}, C_{b-C}$), three transformers with a turns ratio of $n : 1$ and leakage inductance L_{lk}, six output rectifying diodes ($D_1 - D_6$), and an output filter (L_o and C_o).

The proposed converter is composed of two separate sub-converters in its topology: a six-switch three-phase AC-DC converter that will be referred to as the AC-DC sub-converter and a three-phase full-bridge (FB) DC-DC converter that will be referred to as the DC-DC sub-converter. Switches are shared between the AC-DC and DC-DC sub-converters.

The key element of this design is that the two sub-converters work with different frequency components of the waveform. The AC-DC sub-converter operates based on the low-frequency component of the voltage at converter terminals (A, B, and C) and the DC-DC sub-converter operates with high-frequency voltage components at the converter terminals (A, B, and C); thus, the two converters can be analyzed as two decoupled converters.

The circuit diagram of each sub-converter is shown in Fig. 3. In the following section, the operation of each sub-converter is briefly explained, then the operation of the overall converter is explained.

A. AC-DC SUB-CONVERTER
The AC-DC sub-converter (Fig. 3(a)) is a six-switch VSC. Like conventional VSCs, the AC side of the AC-DC sub-converter is connected to an AC voltage source (the PMSG), but the DC side is floating. The AC-DC sub-converter operates as a current-controlled voltage source. This means that the AC-DC sub-converter generates a three-phase sinusoidal voltage with respect to the modulation signals (m_{abc}), as shown in Fig. 4(a). The input current is controlled so that the active power generated by the PMSG is converted to DC power and stored in the intermediate DC bus capacitor (C_1). Moreover, the reactive power exchange between the PMSG and the AC-DC sub-converter is set to zero to minimize the power losses in the PMSG and the converter. In order to implement such a strategy, the decoupled power control method in the rotor synchronous reference frame (dq-frame) is used [27].
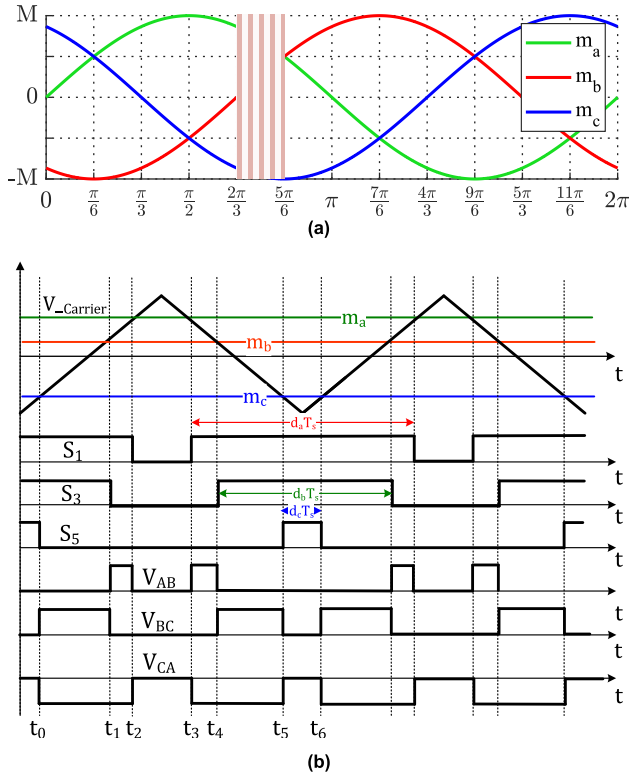
FIGURE 4. Converter waveforms. (a) modulation signals, (b) modulation signals, carrier, duty cycles and voltages waveforms.

FIGURE 5. Closed-loop current controller for d and q axes current components $x \in (d,q)$.

the PI controller parameters of a VSC are explained in detail in [28].

B. DC-DC SUB-CONVERTER

The DC-DC sub-converter (Fig. 3(b)) is a three-phase PWM full-bridge (PWM-FB) DC-DC converter and has the same topology as the one proposed in [29]. The difference between the converter proposed in [29] and the DC-DC sub-converter is in their operation methods. In the former converter, the duty cycle of the converter switches are set by the output voltage controller, but in the latter converter, the duty cycle of the converter switches are set by the AC-DC sub-converter controller.

As stated, the DC-DC sub-converter transfers energy from the intermediate DC bus capacitor (C_1) to the output by using the high-frequency components of the voltage waveforms at point A, B, and C; thus, the DC-DC sub-converter operation can be explained based on the waveforms of the voltage over the switching cycle (Fig. 4(b)). Fig. 4(b) shows the modulation signal, the carrier signal, associated gating signals, and the voltage across the converter terminals (V_{AB}, V_{BC}, V_{CA}) over the switching frequency, in the shaded area of Fig. 4(a). It should be noted that the gating signal of the lower switch of each leg is complementary to that of the corresponding upper switch of the same leg, with an appropriate dead-time inserted to avoid any shoot-through.

As can be seen from (Fig. 4(b)), the terminal voltages are a square waveform and a DC component across point A-B, B-C, and C-A. A DC blocking capacitor blocks the DC component of each square wave and the AC components are applied to the appropriate transformer primary winding.

The AC component passes through the transformers, and after rectification, a low pass LC filter removes the switching frequency components from the voltage. The output LC filter is designed to prevent the inductor current dropping to zero (continuous conduction mode). This condition will reduce the current stress on the converter components and make the output current smoother.

Under these conditions, DC-DC sub-converter modes of operation can be derived. The modes of operation are explained for a set of typical modulation signals between ($2\pi/3 < \omega t < 5\pi/6$). The equivalent circuit associated with each mode is shown in Fig. 6. It should be noted that the DC-MG is modeled with its Thevenin equivalent circuit, which includes a Thevenin voltage source (V_{DC-MG}) and Thevenin resistance (R_{DC-MG}). The blocking capacitors block the phase- to-phase low-frequency component of the voltage; thus, at t_0, the relation between blocking capacitor

As stated, the power transfer in the AC-DC sub-converter happens through the low-frequency component of the voltage and current; thus average voltage equations are used to model the operation of the AC-DC sub-converter. The KVL equations in the stator in the dq-frame can be expressed as

$$L_s \frac{di_{qs}}{dt} = V_{qs} - R_s i_{qs} - \omega_g p (L_s i_{ds} + \psi) \quad (1)$$

$$L_s \frac{di_{ds}}{dt} = V_{ds} - R_s i_{ds} + \omega_g p L_s i_{qs} \quad (2)$$

where V_{qs}, V_{ds}, I_{qs}, and I_{ds} are the q-axis and d-axis components of the stator voltages and currents in the rotor dq-frame, respectively. L_s is the stator inductance, R_s is the stator resistance, ω_g is the PMSG angular speed, ψ is the magnetic flux of the permanent magnets, and p is the number of the PMSG pole pairs.

The control equation can be derived from (1) and (2) as follows:

$$L_s \frac{di_{qs}}{dt} + R_s i_{qs} = u_{qs} \quad (3)$$

$$L_s \frac{di_{ds}}{dt} + R_s i_{ds} = u_{ds} \quad (4)$$

As can be seen from (3) and (4) the control equations for the AC-DC sub-converter are the same as those of a conventional VSC. The control structure for each current component is shown in Fig. 5. A PI controller is used in each loop to control the current at the converter terminals. The design details for
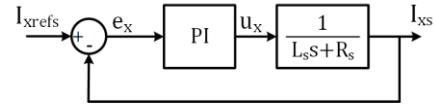
voltages are $V_{Cb-B(t0)} > V_{Cb-A(t0)} > 0 > V_{Cb-C(t0)}$ and $|V_{Cb-C(t0)}| > |V_{Cb-B(t0)}| > |V_{Cb-A(t0)}|$.

Mode 1 ($t_0 < t < t_1$): At the start of this mode, switch S_5 is turned off. The converter terminal voltages are as follows: V_{AB} is equal to zero, V_{BC} is equal to $+V_{dc}$, and V_{CA} is equal to $-V_{dc}$. As a result, V_{Pri-A} is equal to $(-V_{Cb-A})$, V_{Pri-B} is equal to $(V_{dc} - V_{Cb-B})$, and V_{Pri-C} is equal to $(V_{dc} + V_{Cb-C})$. Since the primary of T_B is exposed to the highest positive voltage and the primary of T_C is exposed to the highest negative voltage, the secondary side current exits from T_B and flows through D_3 and returns through D_2 to T_C. The transformers are wye-connected at the secondary side so that the transformer primary currents are the same (I_{Lo}/n). C_{b-B} is charged and C_{b-C} is discharged according to the direction of the primary currents.

Mode 2 ($t_1 < t < t_2$): At the start of this mode, switch S_3 is turned off. The converter terminal voltages are as follows: V_{AB} is equal to $+V_{dc}$, V_{BC} is equal to 0, and V_{CA} is equal to $-V_{dc}$. As a result, V_{Pri-A} is equal to $((V_{dc} - V_{Cb-A})$, V_{Pri-B} is equal to $(-V_{Cb-B})$, and V_{Pri-C} is equal to $(V_{dc} + V_{Cb-C})$. Since the primary winding of T_A is exposed to the highest positive voltage and the primary winding of T_B is exposed to the highest negative voltage, secondary side current exits from T_A and flows through upper diodes D_1 and returns through T_B, through lower diode D_6. C_{b-A} is charged and C_{b-B} is discharged according to the direction of the primary currents.

Mode 3 ($t_2 < t < t_3$): At the start of this mode, switch S_1 is turned off. The converter terminal voltages are equal to zero in this mode. According to blocking capacitor voltages, the primary of T_C is exposed to the highest positive voltage and the primary of T_B is exposed to the highest negative voltage so that the secondary side current exits from T_C, flows through upper diodes D_5 and returns through T_B, through lower diode D_6. C_{b-C} is charged and C_{b-B} is discharged according to the direction of the primary currents.

Mode 4 ($t_3 < t < t_4$): At the start of this mode, S_1 is turned off. This mode is the same as Mode 2.

Mode 5 ($t_4 < t < t_5$): At the first of this mode, switch S_3 is turned off. This mode is the same as Mode 1.

Mode 6 ($t_5 < t < t_6$): At the first of this mode, switch S_5 is turned off. This mode is the same as Mode 3.

C. CONVERTER DESIGN PROCEDURE

The design of several key converter components such as the blocking capacitors and the output filter was explained in detail in [26] and thus wil not be explained in this paper. In this section, only the procedure for selecting the transformer turns ratio and switch ratings will be explained.

1) TRANSFORMER TURNS RATIO

As shown in Fig. 4(b), the voltage across the transformer's primary winding is the same as that of a standard full-bridge converter so that the same design procedure as the one presented in [30] can be used to design the transformer. The main parameter needed to design the transformer is the turns-ratio

and the selection of a turns-ratio value can be done according to the following procedure.

Based on an analysis of the DC-DC sub-converter, V_{C_o} is a function of the intermediate DC bus voltage (V_{bus}), the modulation index (M), and the turns-ratio of the transformer (n). M is governed by the AC-DC sub-converter control equations; thus, V_{bus} and n are the key design parameters in this procedure. Since V_{bus} is limited by the voltage rating of the converter switches, n is expressed based on the converter parameters.

The modulation index can be determined by solving (1) and (2) under steady-state operatingon conditions as follows:

$$m_q = \frac{2\omega_g p\psi}{V_{bus}} \tag{5}$$

$$m_d = \frac{2}{V_{bus}}(\omega_g pL_s\hat{I}_a) \tag{6}$$

where $\hat{I}_a$ is the peak value of the PMSG phase current. It should be noted that I_{ds} is set to zero by the controller to perform PFC.

The value of V_{bus} is a design parameter and should be chosen so that the values of M_d and M_q meet the PWM linear operation condition at the converter rated power, according to

$$M = \sqrt{M_d^2 + M_q^2} < 1 \tag{7}$$

Based on Fig. 4(b), a unipolar double-edge carrier signal is used to generate PWM signals. The double Fourier analysis method is used to decompose the converter terminal voltage waveforms (V_{AB}, V_{BC}, and V_{CA}) [31]. Since a single carrier signal is used for all modulation signals, the switching frequency harmonic and triplen (odd multiples of the third harmonic) sideband switching harmonics do not appear in the harmonic contents of V_{AB}, V_{BC}, and V_{CA}. The terminal voltage Fourier transform for V_{AB} can be expressed as

$$
\begin{aligned}
V_{AB} = V_{bus} &\left\{ \frac{1}{2} + \frac{\sqrt{3}\,M}{2}\cos\left(\omega_e t - \frac{\pi}{6}\right) \right. \\
&+ \sum_{x=1}^{\infty}\sum_{y\in U_1} \frac{2\sqrt{3}}{x\pi} J_x\left(\frac{Mx\pi}{2}\right)\sin\left(\frac{(x+y)\pi}{2}\right) \\
&\times \cos\left[(\omega_c t + \theta_c) + y\left(\omega_e t - \frac{\pi}{6}\right)\right] \\
&+ \sum_{x=1}^{\infty}\sum_{y\in U_2} \frac{2\sqrt{3}}{x\pi} J_x\left(\frac{Mx\pi}{2}\right)\sin\left(\frac{(x+y)\pi}{2}\right) \\
&\left. \times \cos\left[(\omega_c t + \theta_c) + y\left(\omega_e t + \frac{\pi}{6}\right)\right] \right\}
\end{aligned} \tag{8}
$$

where ω_e is the angular frequency of the PMSG terminal voltage, ω_c is the angular frequency of the carrier signal, θ_c is the initial phase of the carrier signal, J_x is a Bessel function of the first kind, $U_1 = \{\pm(3k-2)|k \in \mathbb{N}\}$, and $U_2 = \{\pm(3k-1)|k \in \mathbb{N}\}$. The harmonic contents of V_{BC} and V_{CA} waveforms are the same; only $\pi/6$ is replaced by $-\pi/2$ and $-7\pi/6$, respectively.
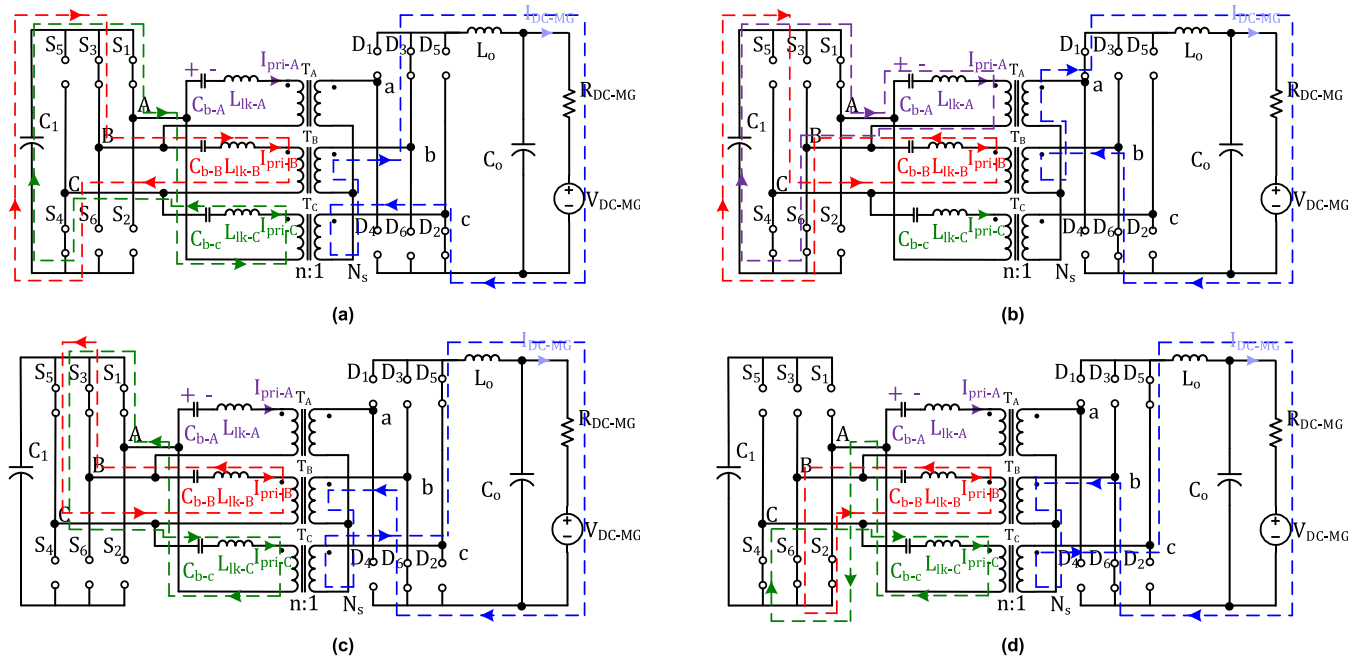
FIGURE 6. DC-DC converter modes of operation. (a) mode 1 & 5, (b) mode 2 & 4, (c) mode 3, (d) mode 6.

Blocking capacitors block the dc and low-frequency components of (8) and high-frequency components pass through the transformer, thus, the secondary voltage of T_A can be written as

$$
V_{aNs} = \frac{V_{bus}}{n} \left\{ \sum_{x=1}^{\infty} \sum_{y \in U_1} \frac{2\sqrt{3}}{x\pi} J_x \left(\frac{Mx\pi}{2} \right) \sin \left(\frac{(x+y)\pi}{2} \right) \right.
$$
$$
\times \cos \left[(\omega_c t + \theta_c) + y \left(\omega_e t - \frac{\pi}{6} \right) \right]
$$
$$
+ \sum_{x=1}^{\infty} \sum_{y \in U_2} \frac{2\sqrt{3}}{x\pi} J_x \left(\frac{Mx\pi}{2} \right) \sin \left(\frac{(x+y)\pi}{2} \right)
$$
$$
\left. \times \cos \left[(\omega_c t + \theta_c) + y \left(\omega_e t + \frac{\pi}{6} \right) \right] \right\} \quad (9)
$$

According to (9), the secondary voltage of the transformers can be decomposed to two sets of three-phase voltage, one set for each sideband of the harmonics of the switching frequency. These three-phase voltages are rectified and pass through an LC filter. The RMS value of the transformer secondary voltage can be calculated by adding the square root of the RMS value of each harmonic voltage as follows:

$$
V_{aNs-RMS}
$$
$$
= \frac{V_{bus}}{n} \sqrt{ \sum_{x=1}^{\infty} \sum_{y \in U_1 \cup U_2} [\frac{\sqrt{6}}{x\pi} J_x \left(\frac{Mx\pi}{2} \right) \sin \left(\frac{(x+y)\pi}{2} \right)]^2 }
$$
$$
= \frac{V_{bus}}{n} \gamma(M) \quad (10)
$$

The RMS voltage of the harmonics has an inverse relation with the harmonic number (x); thus, 20 harmonics are

considered to calculate the value of $\gamma(M)$ to limit the calculation error to less than 5%. A value of $\gamma(M)$ has been determined for various values of M, as shown in Fig. 7, by using MATLAB software.
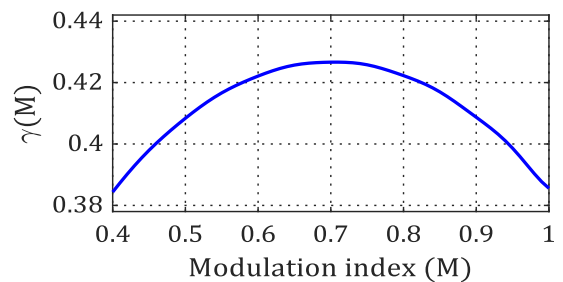

FIGURE 7. The value of $\gamma(M)$ in (11).

The output converter voltage can be determined by using the three-phase rectifier equations in [32], as follows:

$$
V_{C_o} = \frac{V_{bus} 3\sqrt{6}}{n\pi} \gamma(M) = \frac{V_{bus} D_{eff}}{n}
$$
$$
D_{eff} = \frac{3\sqrt{6}}{\pi} \gamma(M) \quad (11)
$$

The value of transformer's turns ratio can be selected according to

$$
n = \frac{V_{bus} D_{eff}}{V_{C_o}} \quad (12)
$$

The value of V_{bus} is selected according to (5), (6), and (7) and the value of $\gamma(M)$ can be found from Fig. 7.

2) SWITCH PARAMETERS

The converter switches should block the voltage of V_{bus} when they are turned off; as a result, the peak voltage rating of the switches is V_{bus}. The current ratings of the switches are calculated in [26]. It should be noted that since switches in the converter are shared by the AC-DC and DC-DC sub-converter stages, the current ratings of the switches are higher than those of conventional two-stage converters.

The design procedure for an example 10kW WECS that is integrated into a 380VDC microgrid is as follows: The specifications of PMSG for a typical 10kW WECS have been taken from the model used in [33]. The parameters of the PMSG are listed in Table 1.

TABLE 1. Simulated system parameters.

Symbol	Quantity	Value
P_{PMSG}	PMSG rated power	10kW
V_{ll}	PMSG rated line to line voltage	380 V
R_s	Stator resistance	0.5 Ω
L_s	Stator leakage inductance	4.48 mH
p	PMSG pole pairs	19
ψ	Flux linkage established by permanent magnets	0.39 V.s
F_{sw}	Isolated single-stage AC-DC converter switching frequency	20 kHz
$V_{DC\text{-}MG}$	DC microgrid rated voltage	380 V
P_T	Turbine rated power	10kW
N_t	Turbine number of blades	3
	Turbine rotor radius	2.9 m
	Turbine airfoils	S822, S823
	Turbine hub height	34.6 m
	Turbine pitch angle	0º
	Turbine cut-in wind speed	4 m/s
	Turbine rated wind speed	11 m/s
	Turbine cut-out wind speed	30 m/s
	Turbine optimal tip speed ratio (λ_{max})	5.7
	Turbine maximum power coefficient ($C_{p,max}$)	0.48
	Turbine total moment of inertia (J)	7.71 kg.m^2
	Turbine rotor angular speed	190 RPM

The converter can be designed as follows:

- The maximum intermediate DC voltage (V_{bus}) has been chosen to be 800V so that 1.2kV SiC devices can be used with a 50% safety margin.
- The maximum value of M can be determined from the AC-DC converter equations ((5) and (6)) and is equal to 0.96, which results in $\gamma (M) = 0.382$ according to the graph in Fig. 7. (CHECK THE FIG. NUMBER)
- Using (11), the value of the effective duty cycle for the DC-DC stage D_{eff} can be found to be 0.89.
- The transformer turns ratio n can then be found from (12) and is equal to 1.8 for this example.
- The RMS switch current can be determined from [26] and found to be 16A, which is higher than that of the switches of the AC-DC stage in a similar two-stage converter, which is 10A.

D. LOSS ANALYSIS

In this section, the converter power losses are discussed and compared with those of a conventional two-stage AC-DC converter. Since the passive components and transformers are the same in both the converters, only the power losses in the converter switches are investigated in this section.

The power losses in the switches of the converter can be expressed as a summation of the switching power losses, which are essentially turn-on power losses in MOSFETs and conduction power losses [34], as follows:

$$P_{loss} = P_{sw} + P_{cond} = \frac{1}{2}V_{on}^2 C_{oss}F_{sw} + I_{rms}^2 \times R_{ds} \quad (13)$$

where V_{on}, is the voltage across the switch at turn-on time, and C_{oss} is the output capacitance of the switch, and F_{sw} is the switching frequency. I_{rms} is the RMS value of the current of the switch as determined in [26], and R_{ds} is the switch resistance.

As shown in [26], with a proper design, $V_{turn-on}$ can be reduced to zero by using the reflected output current; thus, the converter switches work with zero voltage switching (ZVS) and switching power losses are negligible, which offsets the higher conduction losses of the proposed AC-DC converter. This feature lets the converter operate with a relatively high frequency without significant switching power losses. In conventional two-stage converters, the DC-DC converter switches are operated with ZVS and the switching frequency can be high without high power losses, but the AC-DC converter switches work without ZVS so that the switching power losses of these switches are considerable. Moreover, the input power is processed twice by a two-stage AC-DC converter. By simulating the converter as designed in the design example with C2M0025120D switches in PSIM software, the proposed converter was found to have an efficiency of 90% compared to an overall efficiency for a two-stage converter is 92%. It should be noted, however, that the proposed converter is significantly less expensive than a two-stage converter and smaller as well. If the converter's switching frequency is decreased, then its size can be increased to match that of a two-stage converter and it can have comparable efficiency at a lower cost.

III. WECS CONTROL WITH THE PROPOSED CONVERTER

In this section, the control system of a WECS implemented with the proposed converter is explained. The control system is developed based on the mathematical model of the WECS components, including the proposed isolated single-stage AC-DC converter, PMSG, and wind turbine.

The WECS unit control system is shown in Fig. 8. The control system is designed to meet the control objectives discussed in Section 1. In order to do so, an outer loop is used to perform the MPPT and power regulating control and an inner loop is used to perform PFC and actuate the outer loop command value. The operation of the outer and inner loops is explained in the following sections.

A. OUTER CONTROL LOOP

The outer loop consists of the PMSG speed reference generator and speed controller blocks that are shown in Fig. 8.
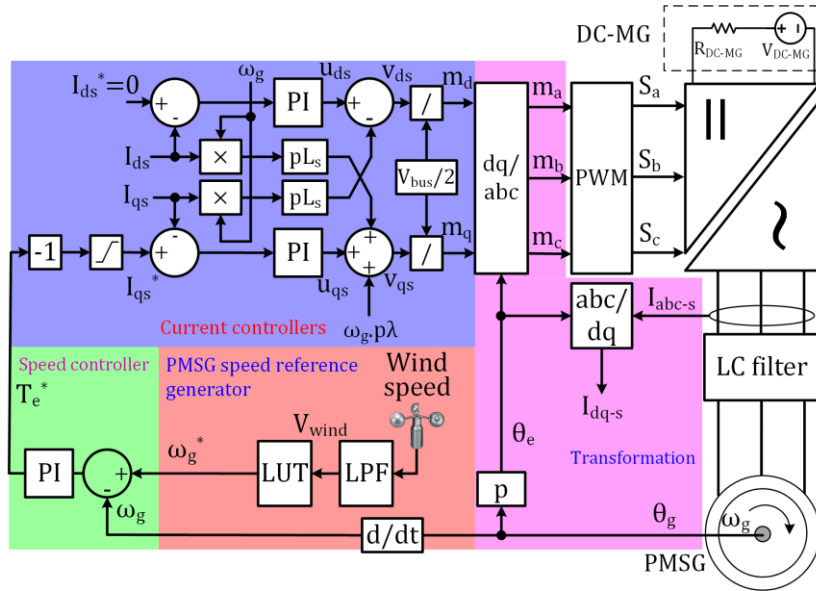
FIGURE 8. WECS unit control system.

The objective of the outer control loop is to control the WECS unit in two different modes. First, when the input wind power is smaller than the wind turbine and the PMSG rated power, the outer loop controller performs MPPT control; this mode is referred to as Region 2 of the WT characteristics. Second, when the input wind power is larger than the wind turbine and the PMSG rated power, the outer loop controller limits the wind power absorbed by the wind turbine and the rated PMSG power (power regulating mode); this mode is referred to as Region 3 of the WT characteristics.

The control for each region can be implemented by using different methods [35]. MPPT in Region 2 can be implemented using various algorithms such as tip speed ratio (TSR) algorithm [36], [37], optimal torque algorithm [38], power signal feedback [39], perturb and observe algorithm [40], fuzzy-based [41], and neural network (NN)-based algorithms [42]. In this paper, the TSR algorithm is used to implement MPPT in Region 2. For Region 3 of operation, various methods such as pitch control [43], stall control [44], yaw [33], and furl [45] can be used. In the present study, stall control is used as the literature shows its advantages over other methods such as yaw and furl for small-scale wind turbines; however, any other control method that has been proposed in the literature can be implemented in Region 2 and Region 3 using the proposed converter. The control methods used in this paper for Region 2 and Region 3 will be briefly explained in this section.

The absorbed power absorbed by the WT can be expressed as:

$$P_{WT} = 0.5\rho A C_p V_{wind}^3 \qquad (14)$$

where ρ is the air density, A is the WT swept area (πr^2, r is the WT radius), C_p is the power coefficient, and V_{wind} is the

wind speed. The value of C_p is the critical factor in controlling the power absorbed by the WT.

When the wind speed is in Region 2, the value C_p should be selected as the largest value that allows MPPT to be performed and in Region 3, the value of C_p should be selected so that the power absorbed by the WT remains constant.

Given this context, the value of C_p is a function of blade pitch angle β, and the ratio of WT angular speed to wind speed is called tip speed ratio. The relation between WT angular speed and wind speed ($\omega_g^* - V_{wind}$) is determined from the design characteristic of WT, such as shown in Fig. 9(a).

In Region 3, the proposed converter forces the blades to operate in the stall region to limit the power absorbed. Stall is an aerodynamic phenomenon and it can happen if the angle of attack (the angle between the chord line and the relative wind speed) exceeds a critical value. When the blades operate in the stall condition, airflow is separated from the upper surface of the blades so that the lift forces on the blades are reduced and power captured is limited. As a result, stall control can be achieved if the blades are appropriately designed for stall regulation and the rotor speed is controlled based on the second part of the ($\omega_g^* - V_{wind}$) curve at wind speeds higher than the rated wind speed,.

A look-up table (LUT) is used in the control system to determine the reference angular speed value for the turbine and generator (ω_g^*) with respect to the wind speed (V_{wind}). Fig. 9(b) shows a graph of C_p and P_{WT} vs wind speed for a WT operating with the stated control method. It should be noted that a low pass filter (LPF) is used to remove small instantaneous fluctuations of wind speed and on the angular speed reference signal.

The angular reference speed of WT (ω_g^*) is compared with the measured speed from the PMSG shaft. The error signal
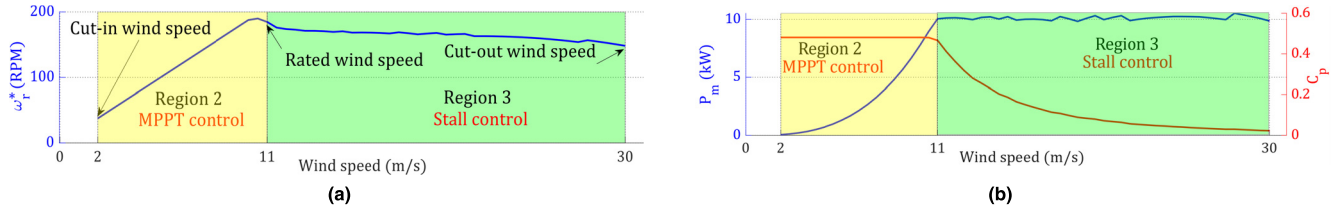
FIGURE 9. WT characteristic and output power, (a) $\omega_g^* - V_{wind}$, (b) $P_m - V_{wind}$ and $C_p - V_{wind}$.

is fed to a PI controller (speed controller) to generate one of the reference values for the inner loop. The following state equations for the mechanical system can be used to design the speed controller:

$$\frac{d\omega_g}{dt} = \frac{T_e - T_f - F\omega_g - T_r/n_{GB}}{J} \quad (15)$$

$$\frac{d\theta_g}{dt} = \omega_g \quad (16)$$

where T_e is the mechanical torque of the PMSG, T_f is the shaft static friction torque, F is the viscous friction coefficient, θ_g is the PMSG shaft position, and J is the mechanical system momentum of inertia. The control variable for the speed control loop is T_e. A limiter block is used to limit T_e to the rated value and ensure the power absorbed by the WT does not exceed the converter ratings.

B. INNER CONTROL LOOP
The inner loop has PI controllers in the synchronous rotor reference frame (dq-frame) to shape the PMSG current based on (1) and (2), as shown in Fig. 8. The objective of this loop is to control the electrical torque of the PMSG (T_e) at a specific value that is specified by the outer loop (T_e^*) while simultaneously performing power factor correction (PFC). According to these conditions, the setpoint values for the q and d axis currents can be calculated as follows:

- Since the q-axis is aligned with the phase 'A' voltage induced by the PMSG, the relationship between I_{qs}^* and T_e^* can be expressed as

$$I_{qs}^* = \frac{2}{3} \frac{T_e^*}{p\psi} \quad (17)$$

- Since the current should be in phase with the voltage, the d-axis component of the current should be set to zero ($I_{ds}^* = 0$).

As stated in Section II.A, a PI controller is used to implement the inner loop current controllers. The modulation signals in dq-frame can be determined by using (3) and (4), as follows:

$$m_d = \frac{2}{V_{bus}}(u_{ds} - \omega_g p L_s I_{qs}) \quad (18)$$

$$m_q = \frac{2}{V_{bus}}(u_{qs} + \omega_g p(L_s I_{ds} + \psi)) \quad (19)$$

IV. EXPERIMENTAL AND SIMULATION RESULTS
In this section, the feasibility of the proposed converter is confirmed by a scaled-down prototype and tested as a single

unit. The performance of the complete WECS is confirmed by simulations of the aerodynamic, mechanical, and electrical systems in MATLAB/SIMULINK.

A. EXPERIMENTAL RESULTS
A scaled-down proof-of-concept prototype of the proposed converter was built to confirm the converter's feasibility. The following specifications were used to build the prototype: line to line RMS voltage, $V_{LL} = 120$ V, line voltage angular frequency, $\omega_e = 377$ rad/sec, DC microgrid voltage $V_{DC-MG} = 48$ V, converter rated power $P_{conv} = 1$kW, and switching frequency $F_{sw} = 50$ kHz. Switches S_1-S_6 were implemented with IPx60R190P6 MOSFETs and DPG10I400PM devices were used as rectifying diodes (D_1-D_6). The input inductors (L_f) were 1.2 mH, the input capacitors (C_f) were 1.2 μF, the blocking capacitors were $C_b = 680$ nF, and the transformer turns ratio was 5:1. The values of L_o and C_o were 2 mH, and 1 mF, respectively. The converter was implemented with the same controller that was discussed in Section 3 and with double edge carrier conventional SPWM, using the slave DSP of a dSPACE 1103 (TM320F240).

It was shown in Section 3 that the transient performance of the converter is the same as that of a typical three-phase, six-switch, non-isolated bidirectional AC-DC converter; thus, only steady-state results are presented here.

Fig. 10 shows typical converter waveforms. Fig. 10(a) shows the three-phase input currents. It can be seen that the inner current controllers keep the PMSG current sinusoidal. Fig. 10(b) shows a typical phase (phase A) voltage and current. It can be seen that input voltage and current are in phase since I_d is set to zero, as shown in Fig. 8. Fig. 10(c) shows the output current in the line frequency scale. It can be seen that it is a smooth DC waveform.

B. SIMULATION RESULTS
In this section, the performance of the overall system, including the WT, PMSG, proposed converter, and DC microgrid model is studied. Two studies are presented in this section. First, the dynamic performance of the proposed converter (Fig. 2) is compared to that of a conventional two-stage converter (Fig. 1(b)), from the point-of-view of the wind turbine control system. Second, the proposed converter is integrated into a complete WECS, and its performance under different wind conditions is investigated.
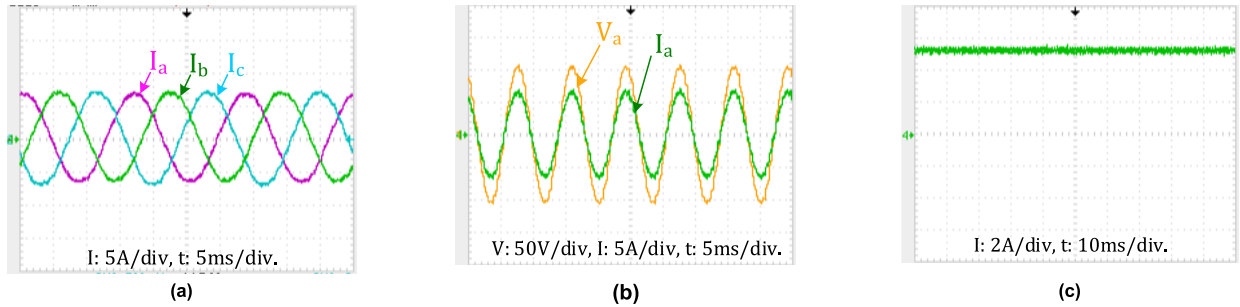
FIGURE 10. Scaled-down prototype waveforms. (a) The AC side currents (I_a, I_b, and I_c), (b) a typical phase voltage and current (phase A), (c) A switch voltage waveform (d) the output current.

1) COMPARISON WITH THE CONVENTIONAL TWO-STAGE CONVERTER

In this study, both the proposed converter and conventional two-stage converter are designed with the specifications shown in Table 1. An input step command power (4 kW-10kW) is applied to both converters and the power absorbed is measured. The controllers are designed according to the procedure presented in [27]. The transfer function of the active power current component (I_{qs}), with respect to its reference value, can be expressed as

$$\frac{I_{qs}(s)}{I_q^*(s)} = \frac{1}{\tau_i s + 1} \tag{20}$$

The value of τ_i is chosen to be 50 μsec. The coefficients of the PI current controllers in Fig. 5 are chosen to be $k_p = 24$, and $k_i = 100$.

Simulation results for both converters are shown in Fig. 11. Fig. 11(a) shows the step response of the proposed converter and Fig. 11(b) shows the step response of the conventional two-stage converter. As can be seen, the dynamic response of both converters is the same, which confirms the discussion in Section II.1. This study demonstrates that any procedure that can be used to control a two-stage converter can be applied to the proposed converter.
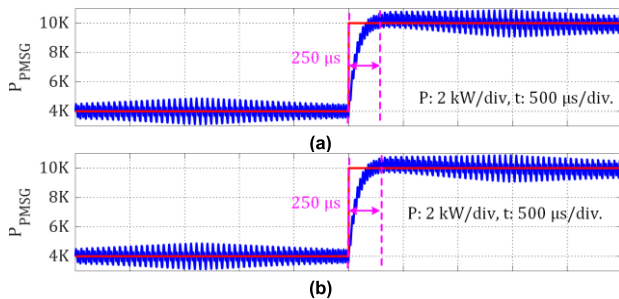

FIGURE 11. Step response for AC input power (a) the proposed converter (Fig. 2), (b) the conventional two-stage converter (Fig. 1(b)).

2) OVERALL WECS UNIT PERFORMANCE WITH THE PROPOSED CONVERTER

In this study, the performance of the overall WECS operation with the proposed converter is examined. This study is performed by simulating the aerodynamic, mechanical, and electrical systems with a unified model. A typical WECS system, such as the system shown in Fig. 1(b), is modeled in the MATLAB/Simulink.

The key parameters of the electrical parts of the WECS were determined in the design example in Section 2. The switching frequency of the converter (F_{sw}) is chosen to be 25 kHz. A three-bladed stall-regulated WT that was designed in [46] by the authors to deliver 10kW rated power is used for this study. The WT is directly connected to the PMSG. The 10kW PMSG is modeled with the same parameters as [33]. The mechanical and electrical system parameters are given in Table 1. The electrical system is modeled with the power system toolbox of MATLAB/Simulink library components and other tools are used to model the mechanical part of the WECS system to assure the mechanical system modeling accuracy. The wind profile is generated by TurbSim [47] and is applied to a WT with $\omega_r^* - V_{wind}$ characteristics that is shown in Fig. 9(a). Aerodynamic forces are calculated by AeroDyn [48] and mechanical forces are calculated by FAST (Fatigue, Aerodynamics, Structures, and Turbulence) software [49].

The aim of the study is to show that the overall WECS system can operate in different modes and that the proposed converter, with isolation, can follow the control system commands to achieve both the MPPT and the power regulation control schemes (shown in Fig. 9) in Regions 2 and 3, respectively. In order to do this, a typical turbulent wind profile with a turbulence intensity of class "b" and an average wind speed of 11 m/s has been generated by TurbSim software based on the IEC 61400-1 standard [50]. The wind profile is applied to the WT and simulation results are shown in Fig. 12.

Fig 12(a) shows the wind profile that is generated by TurbSim software. The wind profile is selected to cover both Regions 2 and 3 of WT operation. The wind profile is applied to the WECS system as an input.

Fig 12(b) shows the angular speed of the WT and PMSG. The reference speed is generated based on the characteristic of the WT that is shown in Fig. 9. It can be seen that when the wind speed is in region 3, the WT is reduced to limit the absorbed power by the WT. When the wind speed is in region 2, the WT speed varies proportionally with wind speed to perform MPPT.
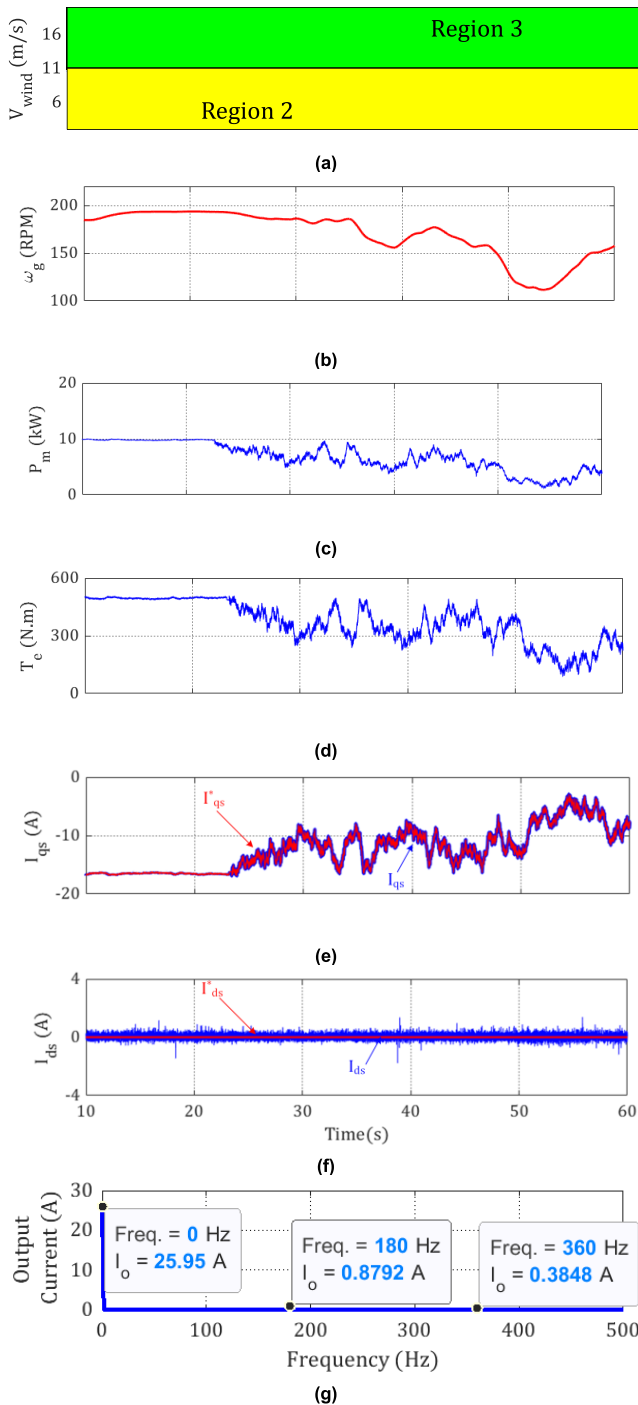
FIGURE 12. Simulation results. (a) Wind speed profile with average of 11m/s and class 'b' turbulence, (b) The PMSG shaft speed, (c) PMSG generated power, (d) PMSG electrical torque (Te), (e) q-axis component of the PMSG current, (f) d-axis component of the PMSG current, (g) harmonic content of output current.

Fig. 12(c) shows the output power of the PMSG. It can be seen that when the wind speed is in Region 2, the absorbed power by WT is less than the rated current of the PSMG and the WECS works in MPPT mode, however, when the wind speed increases to Region 3, the power absorbed by the WT is

limited to the rated power of the WT and the PMSG (10 kW), and the WECS works in power regulating mode.

Fig. 12(d) shows the electrical torque variations caused by the power absorbed by the WT. This value is used to calculate the current reference value for the q-axis component.

Fig. 12(e) shows the reference signal I_{qs}^* that is calculated from T_e by using (16) and the measured I_{qs} value of the q-axis component of the stator current. It can be seen that measured I_{qs} value follows the reference value that is set by the outer loop in both MPPT and power regulating regions. This means the proposed converter can perform MPPT and power regulating functions in the same way as a conventional VSC.

Fig. 12(f) shows the reference I_{ds}^* and measured I_{ds} values of the d-axis component of the stator current. It can be seen that I_{ds} is always zero; thus, the converter performs power factor correction (PFC).

Fig. 12(g) shows the harmonic content of the output current. It can be seen that the output current has a harmonic that is almost 3.3% of its DC component at a frequency that is 6 times the frequency of. It also has a harmonic that is about 1.4% of its DC component at a frequency that is 12 times the frequency of, but this is negligible.

It can be seen from the simulation results that the WECS with the proposed converter can perform all control and optimal operation requirements of a typical WECS.

V. CONCLUSION

This paper proposed a new configuration for interfacing wind energy conversion system (WECS) units to a DC microgrid (DC-MG) that uses a novel AC-DC converter. The new converter is a single-stage AC-DC converter designed for WECS units and its features are as follows:

- The converter provides AC-DC conversion and galvanic isolation with only six active switches.
- The converter performance and control system is very similar to the conventional six switch AC-DC converter; thus, understanding its operation basics and its implementation with standard power electronic blocks is easy.
- The converter can follow MPPT controller command signals in the same way as any two-stage conventional converter; thus, the converter is compatible with most MPPT methods that have been proposed in the literature.
- The converter uses a three-phase six-switch DC-DC converter; thus, the component stress is less than that in single-phase four-switch DC-DC converters.

In this paper, the new configuration of the WECS unit with the new converter is explained. The basic steady-state operation of the new converter is discussed and a dynamic model for the new converter is developed. The feasibility of the converter was confirmed with experimental results from a scaled-down prototype and the overall performance of the WECS unit was studied with simulations that were based on a comprehensive model of the mechanical and electrical parts of the WECS system.

The results for both the converter and the overall WECS confirmed that the proposed converter can be used in small-scale WECSs to reduce the cost and size of the small-scale WECSs that help power a DC microgrid.

REFERENCES

[1] R. H. Lasseter, "MicroGrids," in *Proc. IEEE PESWM*, vol. 1, Jun. 2002, pp. 305–308.

[2] S. Chanda and A. K. Srivastava, "Defining and enabling resiliency of electric distribution systems with multiple microgrids," *IEEE Trans. Smart Grid*, vol. 7, no. 6, pp. 2859–2868, Nov. 2016.

[3] H. Kakigano, M. Nomura, and T. Ise, "Loss evaluation of DC distribution for residential houses compared with AC system," in *Proc. ECCE Asia*, Jun. 2010, pp. 480–486.

[4] T. Dragicevic, J. C. Vasquez, J. M. Guerrero, and D. Skrlec, "Advanced LVDC electrical power architectures and microgrids: A step toward a new generation of power distribution networks," *IEEE Electrific. Mag.*, vol. 2, no. 1, pp. 54–65, Mar. 2014.

[5] T. Dragicevic, X. Lu, J. C. Vasquez, and J. M. Guerrero, "DC microgrids— Part II: A review of power architectures, applications, and standardization issues," *IEEE Trans. Power Electron.*, vol. 31, no. 5, pp. 3528–3549, May 2016.

[6] H. Kakigano, Y. Miura, and T. Ise, "Low-voltage bipolar-type DC microgrid for super high quality distribution," *IEEE Trans. Power Electron.*, vol. 25, no. 12, pp. 3066–3075, Dec. 2010.

[7] K. Sun, L. Zhang, Y. Xing, and J. M. Guerrero, "A distributed control strategy based on DC bus signaling for modular photovoltaic generation systems with battery energy storage," *IEEE Trans. Power Electron.*, vol. 26, no. 10, pp. 3032–3045, Oct. 2011.

[8] H. Kakigano, Y. Miura, and T. Ise, "Distribution voltage control for DC microgrids using fuzzy control and gain-scheduling technique," *IEEE Trans. Power Electron.*, vol. 28, no. 5, pp. 2246–2258, May 2013.

[9] D. Corbus and M. Meadors, "Small wind research turbine final report," Nat. Renew. Energy Lab., Golden, CO, USA, Tech. Rep. NREL/TP-500-38550, Oct. 2005.

[10] K. Strunz, E. Abbasi, and D. Nguyen Huu, "DC microgrid for wind and solar power integration," *IEEE J. Emerg. Sel. Topics Power Electron.*, vol. 2, no. 1, pp. 115–126, Mar. 2014.

[11] S.-Y. Lu, L. Wang, T.-M. Lo, and A. V. Prokhorov, "Integration of wind power and wave power generation systems using a DC microgrid," *IEEE Trans. Ind. Appl.*, vol. 51, no. 4, pp. 2753–2761, Jul. 2015.

[12] Y. Shan, J. Hu, K. W. Chan, Q. Fu, and J. M. Guerrero, "Model predictive control of bidirectional DC–DC converters and AC/DC interlinking converters—A new control method for PV-wind-battery microgrids," *IEEE Trans. Sustain. Energy*, vol. 10, no. 4, pp. 1823–1833, Oct. 2019.

[13] F. Blaabjerg and K. Ma, "Future on power electronics for wind turbine systems," *IEEE J. Emerg. Sel. Topics Power Electron.*, vol. 1, no. 3, pp. 139–152, Sep. 2013.

[14] M. Chinchilla, S. Arnaltes, and J. C. Burgos, "Control of permanent-magnet generators applied to variable-speed wind-energy systems connected to the grid," *IEEE Trans. Energy Convers.*, vol. 21, no. 1, pp. 130–135, Mar. 2006.

[15] M.-H. Ryu, H.-S. Kim, J.-W. Baek, H.-G. Kim, and J.-H. Jung, "Effective test bed of 380-V DC distribution system using isolated power converters," *IEEE Trans. Ind. Electron.*, vol. 62, no. 7, pp. 4525–4536, Jul. 2015.

[16] A. Chub, D. Vinnikov, E. Liivik, and T. Jalakas, "Multiphase quasi-Z-source DC–DC converters for residential distributed generation systems," *IEEE Trans. Ind. Electron.*, vol. 65, no. 10, pp. 8361–8371, Oct. 2018.

[17] *Small-Scale Wind Energy Policy Insights and Practical Guidance*, Carbon Trust, London, U.K., 2008.

[18] M. Narimani and G. Moschopoulos, "A new single-phase single-stage three-level power-factor-correction AC–DC converter with phase-shift modulation," *IEEE Trans. Ind. Electron.*, vol. 60, no. 9, pp. 3731–3735, Sep. 2013.

[19] Y. Jang and M. M. Jovanovic, "The TAIPEI rectifier—A new three-phase two-switch ZVS PFC DCM boost rectifier," *IEEE Trans. Power Electron.*, vol. 28, no. 2, pp. 686–694, Feb. 2013.

[20] T. Zhao, J. Su, J. Wang, D. Xu, and J. Afsharian, "A novel control strategy and commutation method for isolated matrix rectifier," in *Proc. ECCE Asia*, May 2016, pp. 2103–2107.

[21] A. K. Singh, E. Jeyasankar, P. Das, and S. K. Panda, "A single-stage matrix-based isolated three-phase AC–DC converter with novel current commutation," *IEEE Trans. Transport. Electrific.*, vol. 3, no. 4, pp. 814–830, Dec. 2017.

[22] K. Ali, R. Kiran Surapaneni, P. Das, and S. K. Panda, "An SiC-MOSFET-based nine-switch single-stage three-phase AC–DC isolated converter," *IEEE Trans. Ind. Electron.*, vol. 64, no. 11, pp. 9083–9093, Nov. 2017.

[23] Y. Jang, M. M. Jovanovic, M. Kumar, and J. M. Ruiz, "Three-level TAIPEI rectifier—Analysis of operation, design considerations, and performance evaluation," *IEEE Trans. Power Electron.*, vol. 32, no. 2, pp. 942–956, Feb. 2017.

[24] D. S. Wijeratne and G. Moschopoulos, "A novel three-phase buck-boost ac-dc converter," *IEEE Trans. Power Electron.*, vol. 29, no. 3, pp. 1331–1343, Mar. 2014.

[25] M. S. Agamy and P. K. Jain, "A three-level resonant single-stage power factor correction converter: Analysis, design, and implementation," *IEEE Trans. Ind. Electron.*, vol. 56, no. 6, pp. 2095–2107, Jun. 2009.

[26] J. Khodabakhsh and G. Moschopoulos, "A four-switch three-phase AC–DC converter with galvanic isolation," *IEEE Trans. Power Electron.*, vol. 35, no. 2, pp. 1699–1710, Jun. 2019.

[27] A. Yazdani and R. Iravani, *Voltage-Sourced Converters in Power Systems: Modeling, Control, and Applications*. Hoboken, NJ, USA: Wiley, 2010.

[28] P. Rodriguez, J. Pou, J. Bergas, J. I. Candela, R. P. Burgos, and D. Boroyevich, "Decoupled double synchronous reference frame PLL for power converters control," *IEEE Trans. Power Electron.*, vol. 22, no. 2, pp. 584–592, Mar. 2007.

[29] D. S. Oliveira and I. Barbi, "A three-phase ZVS PWM DC/DC converter with asymmetrical duty cycle for high power applications," *IEEE Trans. Power Electron.*, vol. 20, no. 2, pp. 370–377, Mar. 2005.

[30] C. McLyman, *Transformer and Inductor Design Handbook*, 4th ed. Boca Raton, FL, USA: CRC Press, 2011.

[31] F. Vasca and L. Iannelli, *Dynamics and Control of Switched Electronic Systems?: Advanced Perspectives for Modeling, Simulation and Control of Power Converters*. New York, NY, USA: Springer, 2012.

[32] D. W. Hart, *Power Electronics*. New York, NY, USA: McGraw-Hill, 2011.

[33] H. Shariatpanah, R. Fadaeinedjad, and M. Rashidinejad, "A new model for PMSG-based wind turbine with yaw control," *IEEE Trans. Energy Convers.*, vol. 28, no. 4, pp. 929–937, Dec. 2013.

[34] M. Kasper, R. Burkat, F. Deboy, and J. Kolar, "ZVS of power MOSFETs revisited," *IEEE Trans. Power Electron.*, vol. 31, no. 12, pp. 8063–8067, Jun. 2016.

[35] J. F. Manwell, J. G. McGowan, and A. L. Rogers, *Wind Energy Explained?: Theory, Design and Application*. Hoboken, NJ, USA: Wiley, 2002.

[36] V. Yaramasu, A. Dekka, M. J. Durán, S. Kouro, and B. Wu, "PMSG-based wind energy conversion systems: Survey on power converters and controls," *IET Electr. Power Appl.*, vol. 11, no. 6, pp. 956–968, Jul. 2017.

[37] A. M. Knight and G. E. Peters, "Simple wind energy controller for an expanded operating range," *IEEE Trans. Energy Convers.*, vol. 20, no. 2, pp. 459–466, Jun. 2005.

[38] S. Morimoto, H. Nakayama, M. Sanada, and Y. Takeda, "Sensorless output maximization control for variable-speed wind generation system using IPMSG," *IEEE Trans. Ind. Appl.*, vol. 41, no. 1, pp. 60–67, Jan. 2005.

[39] D. Kumar and K. Chatterjee, "A review of conventional and advanced MPPT algorithms for wind energy systems," *Renew. Sustain. Energy Rev.*, vol. 55, pp. 957–970, Mar. 2016.

[40] R. I. Putri, M. Pujiantara, A. Priyadi, T. Ise, and M. H. Purnomo, "Maximum power extraction improvement using sensorless controller based on adaptive perturb and observe algorithm for PMSG wind turbine application," *IET Electr. Power Appl.*, vol. 12, no. 4, pp. 455–462, Apr. 2018.

[41] T. Mahmoud, Z. Y. Dong, and J. Ma, "Integrated optimal active and reactive power control scheme for grid connected permanent magnet synchronous generator wind turbines," *IET Electr. Power Appl.*, vol. 12, no. 4, pp. 474–485, Apr. 2018.

[42] C. Wei, Z. Zhang, W. Qiao, and L. Qu, "An adaptive network-based reinforcement learning method for MPPT control of PMSG wind energy conversion systems," *IEEE Trans. Power Electron.*, vol. 31, no. 11, pp. 7837–7848, Nov. 2016.

[43] H. Geng and G. Yang, "Output power control for variable-speed variable-pitch wind generation systems," *IEEE Trans. Energy Convers.*, vol. 25, no. 2, pp. 494–503, Jun. 2010.

[44] J. Chen, J. Chen, and C. Gong, "New overall power control strategy for variable-speed fixed-pitch wind turbines within the whole wind velocity range," *IEEE Trans. Ind. Electron.*, vol. 60, no. 7, pp. 2652–2660, Jul. 2013.

[45] H. Shariatpanah, R. Fadaeinedjad, and G. Moschopoulos, "An investigation of furl control in a direct-drive PMSG wind turbine," in *Proc. INTELEC*, Sep. 2014, pp. 1–8.

[46] E. Mohammadi, R. Fadaeinedjad, and H. R. Naji, "Flicker emission, voltage fluctuations, and mechanical loads for small-scale stall-and yaw-controlled wind turbines," *Energy Convers. Manage.*, vol. 165, pp. 567–577, Jun. 2018.

[47] B. J. Jonkman, "TurbSim user's guide: Version 1.50," Nat. Renew. Energy Lab., Golden, CO, USA, Tech. Rep. NREL/TP-500-46198, Sep. 2009.

[48] P. J. Moriarty and A. C. Hansen, "AeroDyn theory manual," Nat. Renew. Energy Lab., Golden, CO, USA, Tech. Rep. NREL/TP-500-36881, Jan. 2005.

[49] B. J. Jonkman and M. L. J. Buhl, "TurbSim user's guide: Version 1.50," Nat. Renew. Energy Lab., Golden, CO, USA, Tech. Rep. NREL/EL-500-38230, Aug. 2005.

[50] *Wind Energy Generation Systems—Part 1: Design Requirements*, IEC Standard 61400-1:2019, 2019.

EBRAHIM MOHAMMADI (Member, IEEE) received the B.Sc. degree from the Isfahan University of Technology, Isfahan, Iran, in 2010, and the M.Sc. and Ph.D. degrees from the Graduate University of Advanced Technology, Kerman, Iran, in 2013 and 2018, respectively, all in electrical engineering. He is currently a Postdoctoral Associate with Western University, London, ON, Canada. His research interests include microgrids, renewable energy systems, power quality, and power electronics.

GERRY MOSCHOPOULOS (Senior Member, IEEE) received the B.Eng., M.A.Sc., and Ph.D. degrees in electrical engineering from Concordia University, Montreal, QC, Canada, in 1989, 1992, and 1997, respectively. From 1996 to 1998, he was a Design Engineer with the Advanced Power Systems Division, Nortel Networks, Lachine, QC, Canada. From 1998 to 2000, he was a Postdoctoral Fellow with Concordia University, where he was involved in research in the area of power electronics for telecommunications applications. He joined the Department of Electrical and Computer Engineering, Western University, London, ON, Canada, in 2000, where he is currently a Professor. He has authored or coauthored more than 200 technical articles and one book. He was the Co-Technical Chair of the IEEE International Communications Energy Conference (INTELEC), in 2014, the Co-Technical Chair of the IEEE Canadian Conference on Electrical and Computer Engineering (CCECE), in 2012 and 2014, and the Technical Chair of the IEEE Electrical Power and Energy Conference (EPEC), in 2015. He is an Associate Editor of the IEEE Transactions on Power Electronics and the IEEE Journal of Emerging and Selected Topics in Power Electronics. He is a Registered Professional Engineer in Ontario.

JAVAD KHODABAKHSH (Student Member, IEEE) received the M.Sc. degree in electrical engineering from the University of Tehran, Tehran, Iran, in 2006, and the Ph.D. degree in electrical engineering from Western University, London, ON, Canada, in 2019. From 2007 to 2015, he was a tenured Lecturer with Azad University, Tehran, where he is currently working as an Electrical Design Engineer in various industrial projects (oil and gas and mine and metal), Tehran. He is also a Lecturer with Western University. His research interests include power electronic converters for utility applications, transactive energy, microgrid operation, and renewable energy systems. He is a member of the Ontario Society of Professional Engineers (OSPE).

• • •